J. Ocean Univ. China (Oceanic and Coastal Sea Research)
https://doi.org/10.1007/s11802-019-3873-y
ISSN 1672-5182, 2019 18 (3): 580-588
http://www.ouc.edu.cn/xbywb/
E-mail:xbywb@ouc.edu.cn

Retrieval of Snow Depth on Sea Ice in the Arctic Using the FengYun-3B Microwave Radiation Imager

LI Lele, CHEN Haihua, and GUAN Lei*

College of Information Science and Engineering, *Ocean University of China*, *Qingdao* 266100, *China*

(Received April 7, 2018; revised June 2, 2018; accepted June 22, 2018)

Abstract Snow on sea ice is a sensitive indicator of climate change because it plays an important role regulating surface and near surface air temperatures. Given its high albedo and low thermal conductivity, snow cover is considered a key reason for amplified warming in polar regions. This study focuses on retrieving snow depth on sea ice from brightness temperatures recorded by the Microwave Radiation Imager (MWRI) on board the FengYun (FY)-3B satellite. After cross calibration with the Advanced Microwave Scanning Radiometer-EOS (AMSR-E) Level 2A data from January 1 to May 31, 2011, MWRI brightness temperatures were used to calculate sea ice concentrations based on the Arctic Radiation and Turbulence Interaction Study Sea Ice (ASI) algorithm. Snow depths were derived according to the proportional relationship between snow depth and surface scattering at 18.7 and 36.5 GHz. To eliminate the influence of uncertainties in snow grain sizes and sporadic weather effects, seven-day averaged snow depths were calculated. These results were compared with snow depths from two external data sets, the IceBridge ICDIS4 and AMSR-E Level 3 Sea Ice products. The bias and standard deviation of the differences between the MWRI snow depth and IceBridge data were respectively 1.6 and 3.2 cm for a total of 52 comparisons. Differences between MWRI snow depths and AMSR-E Level 3 products showed biases ranging between −1.01 and −0.58 cm, standard deviations from 3.63 to 4.23 cm, and correlation coefficients from 0.61 to 0.79 for the different months.

Key words MWRI; AMSRE; brightness temperature; snow depth; inter-sensor calibration; sea ice concentration

1 Introduction

The Arctic has attracted much interest among climate researchers because climate-change warming is expected to be amplified 1.5 to 4.5 times in the region, with the high albedo of sea ice and snow depth postulated as a key reason for amplification (Holland and Bitz, 2003; Comiso and Hall, 2014). The thermal conductivity of snow is nearly an order of magnitude smaller than sea ice; therefore, sea ice covered with snow is effectively insulated, which limits the energy and momentum exchange between the atmosphere and surface. In winter, the thermal flow in thick ice is two orders of magnitude smaller than in the open water. Even a thin snow layer will significantly influence the thermal exchange between the atmosphere and surface (Comiso *et al.*, 2003). Snow depth is also an important parameter to consider when calculating the fresh water budget from sea ice and providing accurate rainfall estimates. These considerations have results in greater interest in sea ice and covering snow, potentially the most important parameters in the Arctic when studying the global climate system.

Nevertheless, due to the particular characteristics of the polar environment, there are many challenges to overcome when conducting traditional *in-situ* measurements, such as developing instruments that can provide stable and accurate readings in extremely cold conditions, transporting such instruments, and overcoming the influence of polar night. In contrast, satellite observations have many advantages. They provide consistent, accurate, and integrated data records that can determine various natural phenomena in polar regions. Several satellite sensors have been used to observe the polar regions with a spectral coverage from visible to microwave wavelengths. Compared to infrared and visible radiation, microwaves are more appropriate for monitoring sea ice and snow in polar regions due to their ability to provide all-day and all-weather observations. Passive microwave remote sensing observations of sea ice concentrations have proven crucial in understanding the effects of polar sea ice and snow.

The Electrically Scanning Microwave Radiometer (ESMR), onboard the National Aeronautics and Space Administration of USA (NASA) Nimbus 5 satellite in 1972, was the first passive microwave sensor successfully used for global ice distribution measurements (Gloersen *et al.*, 1974; Parkinson *et al.*, 1987). Since then, several other radiometers have been used to monitor polar sea ice, including the Scanning Multichannel Microwave Radiometer (SMMR) (Gloersen and Barath, 1977; Zwally *et al.*,

* Corresponding author. E-mail: leiguan@ouc.edu.cn

1983), Special Sensor Microwave/Imager (SSMI) (Cavalieri *et al.*, 1992; Comiso *et al.*, 1997; Markus and Cavalieri, 2000), and Advanced Microwave Scanning Radiometer for Earth Observation System (AMSR-E) that released operational sea ice products, including sea ice concentration, sea ice temperature, and snow depth on sea ice (Comiso *et al.*, 2003). Finally, the Advanced Microwave Scanning Radiometer 2 (AMSR2), mounted on the Global Change Observation Mission 1st-Water (GCOM-W1), has been a successor to AMSR and AMSR-E (Markus *et al.*, 2015).

The FengYun-3 (FY-3) satellite series is a second generation of Chinese polar-orbiting meteorological satellite, with substantially enhanced functionality and technical capabilities. They are flown in a circular sun-synchronous near-polar orbit, with an inclination of 98.75° and an orbit period of 101.6 minutes. The Microwave Radiation Imager (MWRI) is one of 11 sensors mounted on the FY-3B satellite, which was launched in November 2010 by the China Meteorological Administration/National Satellite Meteorological Center (CMA/NSMC). It is a total power passive radiometer with observation frequencies at 10.65, 18.7, 23.8, 36.5, and 89 GHz and horizontal and vertical polarizations for each frequency (Yang *et al.*, 2011).

In over 40 years of remote sensing of sea ice, several retrieval algorithms have been developed using brightness temperature measurements to determine the area of sea ice cover based on sea ice concentration (Ivanova *et al.*, 2014), such as the NASA Team 2 (NT2) (Markus and Cavalieri, 2000; Comiso *et al.*, 2003), Bootstrap algorithm (Comiso and Sullivan, 1986), and ARTIST Sea Ice (ASI) (Kaleschke *et al.*, 2001; Spreen *et al.*, 2008) algorithms. Compared to those for sea ice concentrations, snow depth algorithms have been developed more gradually. Only one operational data set for snow depth on sea ice in polar regions has been released, based on AMSR-E brightness temperatures from 2002 to 2011. The base algorithm (AMR-E algorithm) was initially developed using SSM/I brightness temperatures to estimate snow depth on Southern Ocean sea ice (Markus and Cavalieri, 1998), and then applied to first-year sea ice regions in the Arctic. In 2003, it was applied to AMSR-E (Comiso *et al.*, 2003). At present there has been no operational data set for snow depth on sea ice provided by an in-orbit radiometer, including AMSR2 and MWRI. Therefore, developing a snow depth retrieval algorithm, especially based on MWRI, is important for providing operational products.

Considering the insufficiency of accurate *in-situ* data for developing a new algorithm, this study focused on deriving snow depth from FY3B/MWRI brightness temperatures using the established snow depth algorithm. Accordingly, the research method first cross-calibrated the brightness temperature from MWRI to the AMSR-E baseline, then calculated sea ice concentrations using the ASI algorithm, and finally derived snow depth with the AMSR- E algorithm.

2 Data

Four main data sets were used in this study. First, the FY3B/MWRI Level 1 swath brightness temperature record was used as input data to calculate snow depth. Second, the AMSR-E Level 2A Version 3 (V003) global swath spatially-resampled brightness temperatures (Ashcroft and Wentz, 2013) were used as calibration data. Third, snow depths from the IceBridge IDCSI4 data set (Kurtz *et al.*, 2015) was applied to evaluate the retrieved snow depth from FY-3B/MWRI. Finally, snow depths from the AMSR-E Level 3 standard sea ice products (Cavalieri *et al.*, 2014) were used to compare snow depths from the MWRI because it is the only standard snow depth product for sea ice that overlaps in time with the MWRI data.

Two multiyear sea ice data sets were also used in this work as ancillary data to calculate snow depth on sea ice, *i.e.*, the Sea Ice Type and EASE-Grid Sea Ice Age products (Tschudi *et al.*, 2016).

2.1 MWRI Data

The FY3B/MWRI Level 1 swath brightness temperatures were obtained from the NSMC, which archives and distributes three level products. They are stored as orbital swath records, with 28 separate ascending and descending files per day. Every file contains records for 10 channels in their original resolutions at five frequencies with dual polarizations (Yang *et al.*, 2012).

In this study, the brightness temperature data for vertical channels at 18.7, 23.8, and 36.5 GHz, and both the vertical and horizontal channels at 89 GHz were used to calculate snow depth on sea ice in the Arctic.

For inter-sensor calibration, the spatial coverage of this data set was north of 30°N. Temporal coverage was from January 1 to May 31, 2011, providing overlapping data between MWRI and AMSR-E. To further evaluate the algorithm results, MWRI brightness temperatures in 2012 were also used in this study.

2.2 AMSR-E Data

AMSR-E Level 2A global swath spatially-resampled brightness temperature products and AMSR-E Level 3 standard sea ice products were provided by the National Snow and Ice Data Center (NSIDC), which distributes daily, weekly, and monthly Level 1A, Level 2A, Level 2B, and Level 3 data products from the AMSR-E.

The AMSR-E Level 2A product contains brightness temperatures available at a variety of resolutions that correspond to the footprint sizes of the observations. Each swath is packaged with associated geolocation fields. In this study, the spatial resolution of each channel was chosen according to the MWRI data.

The AMSR-E Level 3 standard sea ice products include sea ice concentration generated using the NT2 algorithm, sea ice temperature, and snow depth on sea ice produced from the AMSR-E algorithm. These products, together with AMSR-E calibrated brightness temperatures, were mapped to a standard polar stereographic grid at a spatial resolution of 12.5 km (Markus and Cavalieri, 2008). The spatial and temporal coverages of AMSR-E data sets were the same as the MWRI data for inter-sensor calibration.

2.3 IceBridge IDCSI4 Data

The NSIDC distributes NASA's airborne Operation IceBridge IDCSI4 data, which contains derived geophysical data products, including sea ice freeboard, snow depth, and sea ice thickness measurements in Greenland and Antarctica. They are retrieved from the IceBridge Snow Radar, Digital Mapping System (DMS), Continuous Airborne Mapping by Optical Translator (CAMBOT), and Airborne Topographic Mapper (ATM) data sets. The data were collected as part of Operation IceBridge funded campaigns.

The IceBridge campaigns are conducted on an annually repeating basis. Arctic and Greenland campaigns are conducted during March, April, and May. To match the time period of this study, the data for campaigns from 2011 to 2012 were used. Because the nominal flight altitude of the snow radar is 460 m, the snow depth data has a footprint size of 11 m across track and 14.5 m along-track, and the data are averaged in the along-track direction to a 40 m-length scale.

2.4 Multiyear Sea Ice Data

The sea ice age product is released by NSIDC. It provides weekly estimates of sea ice age for the Arctic Ocean from remotely sensed sea ice motion and sea ice extent derived using data from satellite passive microwave instruments, drifting buoys, and a weather model (Tschudi *et al*., 2016). The data were gridded to a 722 × 722 subset of the 12.5 km Northern Hemisphere Equal Area Scalable Earth Grid.

The sea ice type product is distributed by European Organization for the Exploitation of Meteorological Satellites (EUMETSAT) Ocean and Sea Ice Satellite Application Facility (OSI SAF, www.osi-saf.org). It is derived from passive and active microwave remote sensing data combined in a Bayesian approach. They are computed for both hemispheres on the standard OSI SAF grid at 10 km spatial resolution.

3 Methods and Results

As described above, the AMSR-E snow depth on sea ice algorithm was used to derive the only currently available standard product based on satellite microwave radiometry. The instrumental configurations of AMSR-E and MWRI are similar and have nearly simultaneous satellite overpass and data acquisition times, as shown in Table 1 (Kawanishi *et al*., 2003; Yang *et al*., 2012). Therefore, the AMSR-E sensor was selected as the baseline sensor. Compared to other sensors with different overpass times to MWRI, AMSR-E has spatially and temporally collocated observations, which mitigates the potential brightness temperature differences from diurnal changes in the intercalibration.

The methods used in this work were divided into four steps, which are described as follows.

Table 1 Primary specifications of the Advanced Microwave Scanning Radiometer for Earth Observation System (AMSR-E) and Microwave Radiation Imager (MWRI)

Instrument specification	AMSR-E	MWRI
Satellite platform	AQUA	FY3B
Altitude (km)	705	836
Equator crossing time (local time zone)	1:30 a.m. (descending)	1:30 a.m. (descending)
Antenna size (m)	1.6 (diameter)	0.977 × 0.897
Incident Angle	55	53
Footprint size (km × km)	75 × 43 (69 GHz)	N/A
	51 × 29 (10.65 GHz)	85 × 51 (10.65 GHz)
	27 × 16 (18.7 GHz)	50 × 30 (18.7 GHz)
	32 × 18 (23.8 GHz)	45 × 27 (23.8 GHz)
	14 × 8 (36.5 GHz)	30 × 18 (36.5 GHz)
	6 × 4 (89 GHz)	15 × 9 (89 GHz)
Band width (MHz)	350 (6.93 GHz)	N/A
	100 (10.65 GHz)	180 (10.65 GHz)
	200 (18.7 GHz)	200 (18.7 GHz)
	400 (23.8 GHz)	400 (23.8 GHz)
	1000 (36.5 GHz)	400 (36.5 GHz)
	3000 (89 GHz)	3000 (89 GHz)

Note: N/A, not available.

3.1 Inter-Sensor Calibration

The first step was to cross calibrate the brightness temperature from MWRI to the AMSR-E baseline. Considering the overlap time of the two sensors, five-month orbital swath brightness temperatures records from January 1 to May 31, 2011 were extracted over the Arctic area. Because of the similar configuration and nearly simultaneous satellite overpass times of the two radiometers, a linear equation was used as the calibration formula. The matching time window was set to 30 min.

Comparing the different time periods of matching data, including day, week and month, the month unit was finally selected as the matching period for both descending and ascending records. After data preprocessing, which included eliminating invalid data, such as unreasonable

brightness temperatures, and addressing unique locations, such as coastal points and ice water boundary points, approximately 50 million corresponding data points from each channel were obtained and used to calculate calibration coefficients. Finally, 20 sets of calibration parameters were calculated for each month.

3.2 Sea Ice Concentration

The second step was to calculate sea ice concentration, which is an important parameter in calculating the snow depth on sea ice. In this study, the ASI algorithm was used.

The ASI algorithm was originally developed by the University of Hamburg, Germany, to obtain high spatial resolution sea ice concentrations at the 85 GHz channels of the SSM/I sensor for the marginal sea ice zone (Kaleschke *et al.*, 2001). This is an enhancement of the SVENDSEN algorithm (Svendsen *et al.*, 1987), which was the first algorithm to use high-frequency channels to retrieve sea ice concentration. Compared with other 85 GHz algorithms, such as the Kern algorithm (Kern, 2004), the ASI algorithm has the advantage that no additional data sources are needed as inputs. In 2008, Spreen *et al.* (2008) applied it to the AMSR-E sensor using the 89 Ghz channels as an alternative.

The ASI algorithm is based on the theory that the polarization difference of the emissivity near 90 GHz is similar for all ice types and much smaller than that for open water. This is also true for the polarization difference for brightness temperature because emissivity controls changes in brightness temperatures. Therefore, different surface types can be distinguished using the polarization difference of the brightness temperature at 89 GHz, which is defined as:

$$P = T_B(89V) - T_B(89H)\,, \tag{1}$$

where P is the polarization difference of the brightness temperature at 89 GHz and $T_B(89V)$ and $T_B(89H)$ are the vertical and horizontal brightness temperature at 89 GHz, respectively. The sea ice concentration is assumed to be a function of the polarization difference, calculated as follows:

$$C = a_3P^3 + a_2P^2 + a_1P + a_0\,, \tag{2}$$

where C is sea ice concentration and a_0 to a_3 are the coefficients of the equation, which are calculated from Eq. (3).

$$\begin{bmatrix} P_0^3 & P_0^2 & P_0 & 1 \\ P_1^3 & P_1^2 & P_1 & 1 \\ 3P_0^3 & 2P_0^2 & P_0 & 0 \\ 3P_1^3 & 2P_1^2 & P_1 & 0 \end{bmatrix} \begin{bmatrix} a_3 \\ a_2 \\ a_1 \\ a_0 \end{bmatrix} = \begin{bmatrix} 0 \\ 1 \\ -1.14 \\ -0.14 \end{bmatrix}, \tag{3}$$

where P_0 and P_1 represent the polarization difference of the brightness temperature at 89 GHz in open water and in a region with 100% ice coverage, respectively. In this study, the empirical values of 47 and 11 were used (Spreen *et al.*, 2008).

Because there is an influence from atmospheric cloud liquid water and water vapor on the brightness temperatures at 89 GHz, using these channels to calculate sea ice concentrations can be problematic. To eliminate spurious weather effects over the open ocean, two different weather filters were applied (Spreen *et al.*, 2008). Through the previously described process, all ice concentrations were maintained above 15%, which is defined as the ice edge contour line (Gloersen *et al.*, 1992; Spreen *et al.*, 2008).

After using the weather filter, the sea ice concentrations were projected onto polar stereographic grids with grid cells of 12.5 ×12.5 km at 70° latitude because the projection plane is tangent to the Earth at 70°. Subsequently, the orbital sea ice products were averaged to daily records.

3.3 Daily Snow Depth on Sea Ice

The third step was to derive the snow depth with the AMSR-E algorithm according to the sea ice concentration and proportional relationship between snow depth and surface scattering. The algorithm operates similarly to that of the AMSR-E snow-on-land algorithm (Kelly *et al.*, 2003), which is based on an assumption that scattering increases with increasing snow depth and scattering efficiency is greater at 37 GHz than at 19 GHz. For snow-free sea ice, the gradient ratio is near zero and becomes increasingly more negative as snow depth increases.

According to the proportional relationship between snow depth and surface scattering, the brightness temperatures at 36.5 and 18.7 GHz for the vertical channels were used to regress the snow depth on sea ice (Comiso *et al.*, 2003). The relevant equations are:

$$h_s = 2.9 - 782.4 \times GRV\,, \tag{4}$$

$$GRV = \frac{\left[T_B(36.5V) - T_B(18.7V) - k_1(1-C)\right]}{\left[T_B(36.5V) + T_B(18.7V) - k_2(1-C)\right]}\,, \tag{5}$$

$$k_1 = T_{b0}(36.5V) - T_{b0}(18.7V)\,, \tag{6}$$

$$k_2 = T_{b0}(36.5V) + T_{b0}(18.7V)\,, \tag{7}$$

where h_s is snow depth and T_{b0} is the average value of the brightness temperatures on the different channels for open water.

The snow depth algorithm has several limitations. First, it is applicable to dry snow only. For wet snow, the emissivity at 18.7 and 36.5 GHz is almost identical and snow depth cannot be determined. Second, because the penetration depths of the microwave signals at 36.5 and 18.7 GHz were less than 50 cm, only snow depths under 50 cm were calculated from the algorithm. Finally, the algorithm is only valid for seasonal ice areas in the Arctic.

Using Eqs. (4)−(7), daily snow depths in the Arctic were calculated from daily sea ice concentrations and brightness temperatures from the 18.7 and 36.5 *V* channels.

3.4 Seven-Day Averaged Snow Depth

Because snow usually melts during daytime and freezes at night, the grain sizes become larger. This process causes surface emissivity to decrease much faster at 36.5 GHz than at 18.7 GHz and may overestimate snow depth.

To eliminate the influence of uncertainties from grain size, density variations, and sporadic weather effects, the data retrieved in this study were averaged to obtain seven-day records. While averaging the snow depth, several types of flags were placed into the data, including multiyear sea ice, variable data, and melted snow.

3.4.1 Multiyear sea ice flag

Because the microwave signature between the multiyear sea ice and deep snow are very similar, the snow depth on multiyear sea ice cannot be retrieved unambiguously (Comiso *et al.*, 2003). Therefore, multiyear sea ice points must be marked in the data records.

By comparing and processing the sea ice age products, including the sea ice type products and gradient ratio between 36.5 and 18.7 GHz on vertical channels, a multiyear sea ice flag was derived and used in both the daily snow depth and averaged snow depth records.

3.4.2 Variability flag

As described above, the uncertainties in grain size, density variations, and sporadic weather will affect the microwave signature of snow depth. Therefore, large variations in one point's snow depth over several days would result in a variability flag in the data record.

3.4.3 Snow melt flag

At the onset of melt in spring, the sea ice surface generally loses its true emissivity due to the transformation of snow cover to a surface with high emissivity. This transformation occurs because the imaginary part of the dielectric constant of snow becomes relatively high when it is slightly wet (about 3% liquid). However, the most serious problem for the algorithm is generated from melt ponding effects because the surfaces of melt ponds have signatures of ice free water. Therefore, melt points must be marked in the data record. In this study, the gradient of horizontal and vertical channels on 36.5 Ghz, and differences in brightness temperatures at 23.8 Ghz and 18.7 Ghz were used to distinguish melt and snow points. Then, the melt flags were set in the averaged snow depth.

After all the described steps were complete, the seven-day averaged snow depths were obtained. As an example, Fig.1 shows the snow depth on sea ice on March 23, 2011, which is a seven-day averaged snow depth record from March 17–23, 2011.

4 Discussion

In this study, five months of data from January 1 to May 31, 2011, for FY-3B/MWRI brightness temperatures were processed and seven-day averaged snow depths were derived. To evaluate the snow depth results, two snow depth data sets were used. One was from the IceBridge IDCSI4 data set and the other from AMSR-E Level 3 products.

4.1 Evaluation

Because the spatial resolution of IceBridge IDCSI4 data is 40 m, to facilitate comparisons they were projected and averaged onto the same polar stereographic projection grids as FY-3B/MWRI snow depths. Some data were excluded from the results, including three types of snow depth data flags from MWRI and points higher than 50 cm in the IceBridge data. A total of 52 matching data point sets covered by seasonal ice were obtained where snow depths from both MWRI and IceBridge data were available. These data were collected on March 23, 2011, and the positions are shown with the light green line in Fig.1.

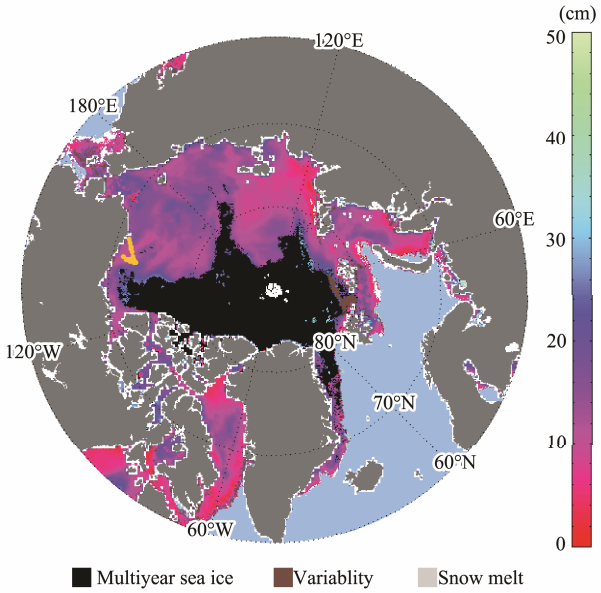

Fig.1 Seven-day averaged snow depths derived from the Microwave Radiation Imager (MWRI) on March 23, 2011. The yellow line in the Beaufort Sea represents the position of the corresponding data (described in Section 4.1) and the white points indicate missing data.

To compare the snow depths derived from calibrated MWRI brightness temperatures (marked MWRI), the other two data sets were compared with the IceBridge data. They contain snow depths derived from uncalibrated MWRI brightness temperatures obtained using the same procedure (MWRI-ORG) and snow depths obtained from AMSR-E Level 3 products (AMSR-E L3).

A quantitative assessment of the differences in snow depth between the three data sets and IceBridge IDCSI4 data (represented by IB) is provided in Table 2. A histogram of the differences and plot of the snow depths are presented in Figs.2 and 3.

The results show that the snow depths from the three data sets were higher than those obtained from the IceBridge IDCSI4 data, with the biases ranging from 1.6 to 3.3 cm, root mean square error (RMSE) values ranging from 3.6 to 4.5 cm, and standard deviations (STD) ranging from 3.1 to 3.3 cm. Therefore, in contrast to snow depths calculated from uncalibrated brightness temperature data at the 52 matchup points, snow depths derived from the calibrated MWRI brightness temperature were more consistent with IceBridge data.

Table 2 Snow depths from three satellite products after subtracting IceBridge IDCSI4 data

Data set	Bias (cm)	RMSE (cm)	STD (cm)	Data set	Bias (%)	RMSE (%)	STD (%)
MWRI-IB	1.6	3.6	3.2	(MWRI-IB)/IB	22	39	32
MWRI-ORG-IB	3.1	4.5	3.3	(MWRI-ORG-IB)/IB	36	51	37
AMSR-E L3-IB	3.0	4.3	3.1	(AMSR-E L3-IB)/IB	32	46	32

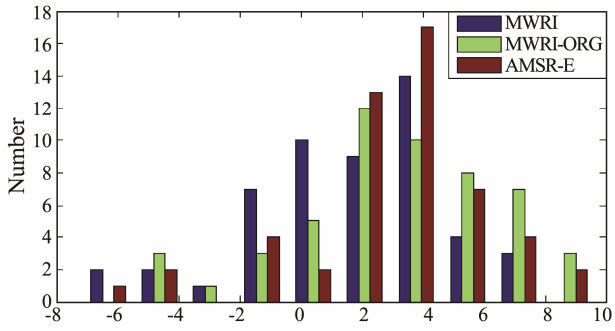

Fig.2 Histogram showing the differences in snow depth results from three satellite products after subtracting the IceBridge IDCSI4 data.

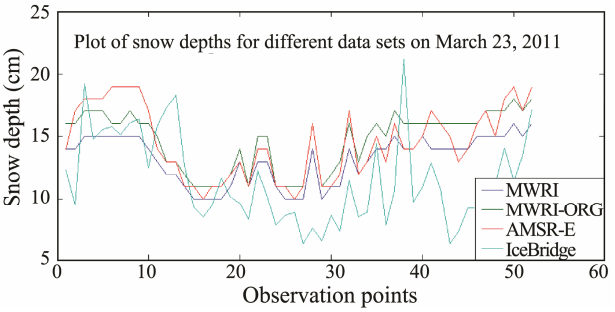

Fig.3 Comparison of snow depth results obtained from four different datasets.

Considering the temporal off-sets between the IceBridge and MWRI, snow depths from the swath brightness temperature of MWRI on March 23, 2011 were calculated together for comparison. A quantitative assessment of the differences in snow depth between the swath data sets and IceBridge IDCSI4 data is provided in Table 3 for 156 matched data points.

As shown in Tables 2 and 3, when compared to the snow depths in the IceBridge data set, the swath data performance is not as good as the averaged snow depth. This difference also indirectly proves the necessity of averaging snow depth.

Because the data-matching in 2011 was insufficient, snow depths from 2012 IceBridge data sets were used to further evaluate the snow depths retrieved in this work.

Comparing Tables 4 and 2, the MWRI snow depth performances were similar in 2011 and 2012.

4.2 Comparison with AMSR-E Level 3 Products

Compared with the large MWRI data coverage in the Arctic, there were few IceBridge data available due to spatial and temporal restrictions in individual campaigns. Therefore, snow depths from AMSR-E Level 3 products were applied as an inter-comparison dataset; the snow depths from AMSR-E Level 3 products on March 23, 2011, are shown in Fig.4.

Comparing Figs.1 and 4, it is clear that the snow depths from calibrated MWRI brightness temperatures are consistent with the AMSR-E Level 3 products in the Arctic. The differences are shown in Fig.5, which were calculated only for valid snow depth points, with all flagged points eliminated.

Fig.5 shows that in some coastal areas, the snow depths obtained in this study were higher than that of the AMSR-E Level 3 products, whereas the opposite was true for some offshore points.

Table 3 Statistical differences in snow depths from calibrated and uncalibrated MWRI swath brightness temperature after subtracting the IceBridge IDCSI4 products

Data set	Bias (cm)	RMSE (cm)	STD (cm)	Data set	Bias (%)	RMSE (%)	STD (%)
MWRI-IB	1.4	4.6	4.0	(MWRI-IB)/IB	28	42	50
MWRI-ORG-IB	3.5	5.5	4.3	(MWRI-ORG-IB)/IB	39	47	61

Table 4 Snow depths from MWRI after subtracting the IceBridge IDCSI4 data from 2012

Data set	Number	Bias (cm)	RMSE (cm)	STD (cm)	Data set	Number	Bias (%)	RMSE (%)	STD (%)
MWRI-IB	713	2.3	5.1	4.5	(MWRI-IB)/IB	713	23	44	37
MWRI-IB(swath)	2651	3.8	5.8	4.5	(MWRI-IB)/IB (swath)	2651	41	41	58

The discrepancies between the snow depths calculated in this study and AMSR-E Level 3 products for each month of our investigation period are provided in Table 5. The comparison shows that the snow depths obtained in this study were generally lower than the AMSR-E Level 3 products in the Arctic. The differences biases were −1.01 to −0.58 cm, while the STD and correlation coefficients ranged from 3.63 to 4.23 cm and 0.61 to 0.79, respectively. The differences were generally consistent over different months.

A histogram of the differences from January 1 to May 31, 2011, was compiled to illustrate the distribution (Fig.6). As shown, the differences between the two data sets were generally symmetrically distributed around a central value of −1 cm, which is consistent with the summarized statistics reported in Table 4.

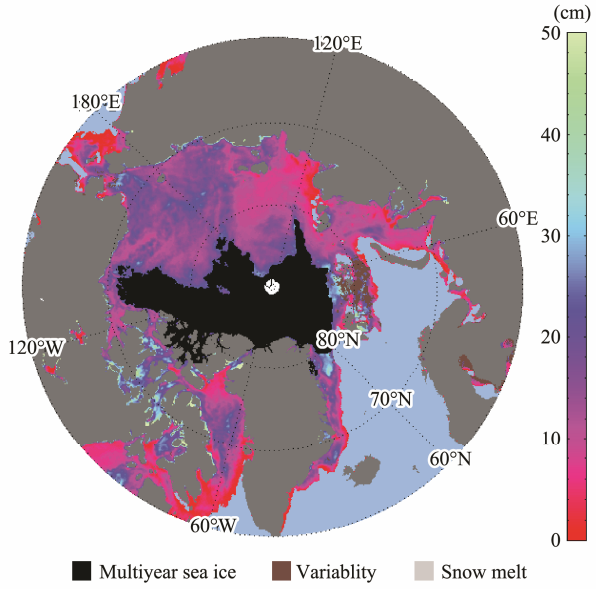

Fig.4 Snow depths obtained from the Advanced Microwave Scanning Radiometer-EOS (AMSR-E) Level 3 on March 23, 2011.

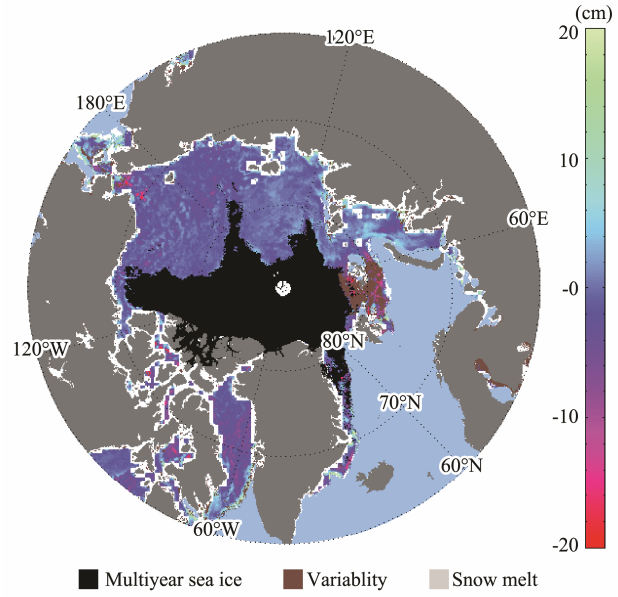

Fig.5 Differences between snow depths on sea ice from Microwave Radiation Imager (MWRI) and Advanced Microwave Scanning Radiometer-EOS (AMSR-E) Level 3 data for March 23, 2011.

Table 5 Statistical evaluation of the snow depth differences between those obtained in this study and the Advanced Microwave Scanning Radiometer-EOS (AMSR-E) Level 3 products

Month	Number	Bias (cm)	STD (cm)	Correlation coefficient
Jan. 2011	1168385	−0.98	4.12	0.68
Feb. 2011	1179452	−0.83	4.23	0.61
Mar. 2011	1364262	−0.68	4.22	0.71
Apr. 2011	1317057	−1.01	4.18	0.77
May. 2011	563993	−0.58	3.63	0.79
All data	5593161	−0.84	4.14	0.73

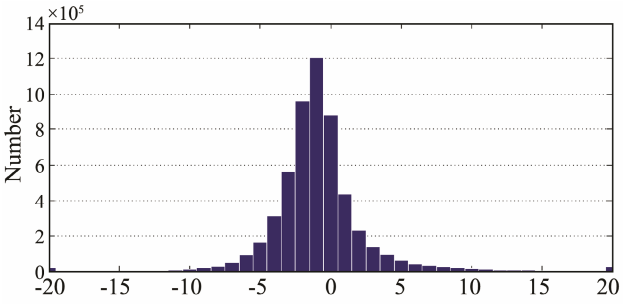

Fig.6 Histogram of the differences in snow depths between MWRI and AMSR-E data from January 1 to May 31, 2011.

4.3 Summary

From the results described in Sections 4.1 and 4.2, the snow depths determined in this study are reasonable and the method viable. Compared to the AMSR-E L3 products, the proposed method showed better performance. However, this conclusion is valid only for the 52 points and does not have universal applicability.

There are several possible reasons for the discrepancies between the snow depths calculated here and IceBridge IDCSI4 data, which are listed as follows:

1) Temporal and spatial off-sets between the IceBridge and MWRI. IceBridge data include values measured over a period of minutes, with a spatial resolution of 40 m, whereas MWRI data is averaged over seven days for accuracy, with a spatial resolution of 12.5 km.

2) Deviations from algorithm coefficients. The AMSR-E algorithm is based on the SSMI data and after cross-calibration from AMSR-E to SSMI, and the same regression coefficients were applied to the AMSR-E brightness temperature and to MWRI, which may generate additional errors.

3) Errors from the sea ice concentration algorithm.

4) Errors from IceBridge data. According to Kurtz *et al.* (2013), the range of snow depth retrievals for IceBridge data was 5–120 cm. Due to a variety of factors, including the finite range resolution of the snow radar (5 cm), density uncertainties, and uncertainty in the detection of the snow-air and snow-ice interfaces, the snow depth uncertainty was set to 5.7 cm.

The differences between the snow depths calculated in this study and the AMSR-E Level 3 products are primarily attributed to sea ice concentration differences. The algorithm used in this study was the ASI algorithm, whereas the AMSR-E Level 3 products were derived from the NT2 algorithm. According to Brucker and Markus (2013), a 5% variation in sea ice concentration will cause variations in snow depths of 1–6 cm. The discrepancies in the sea ice concentrations retrieved from the two algorithms on March 23, 2011, are shown in Fig.7.

As shown in Figs.5 and 7, there is a correlation between the largest snow depth difference and largest difference in sea ice concentration. For example, near the ice edge, sea ice concentrations from ASI algorithm were commonly underestimated than the AMSR-E products, and

would lead to overestimating snow depths in the same areas.

In this study, the second most important contributor to the difference in snow depths was attributed to brightness temperatures. Although the brightness temperatures from the MWRI were calibrated to AMSR-E, the two data sets still deviated. Therefore, snow depths retrieved from them will vary.

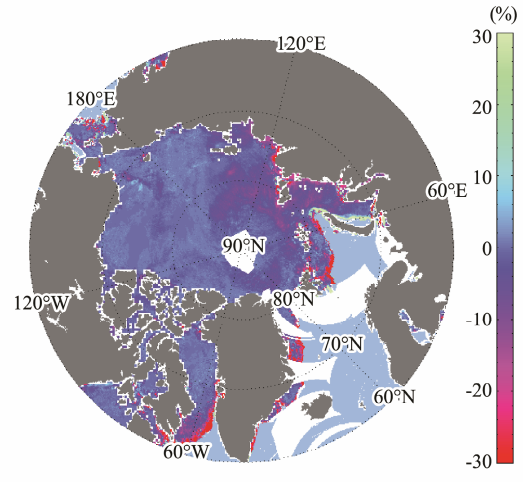

Fig.7 Differences between sea ice concentrations calculated using the Arctic Radiation and Turbulence Interaction Study Sea Ice (ASI) algorithm and NASA Team 2 (NT2) algorithm on March 23, 2011 (white points indicate missing data).

5 Conclusions

In this study, based on the AMSR-E snow depth algorithm and ASI sea ice algorithm, the cross calculated brightness temperatures from MWRI to the AMSR-E baseline were used to calculate the sea ice concentration. Then, daily snow depths on sea ice were retrieved in the Arctic according to the sea ice concentration and proportional relationship between snow depth and surface scattering. Finally, seven-day averaged snow depths were obtained. An evaluation of the snow depths from the IceBridge IDCSI4 data demonstrated that snow depths derived in this study were relatively effective and in better agreement with IceBridge IDCSI4 data than snow depths derived from uncalibrated MWRI. A comparison with the AMSR-E Level 3 sea ice products indicated that the two data sets were generally consistent, with the biases ranging between −1.01 and −0.58 cm and correlation coefficients ranging between 0.61 and 0.79 for each month of the investigation period. Therefore, the method adopted in this study was proven useful for retrieving snow depth on sea ice from MWRI brightness temperatures in the Arctic and has potential for wider use. This study provides the first set of snow depth on sea ice data from MWRI retrieval in the Arctic.

Acknowledgements

The FY-3B/MWRI brightness temperature products used in this study were provided by the NSMC FengYun Satellite Data Center. The IceBridge IDCSI4 data, AMSR-E Level 2A and Level 3 data, and sea ice age data were provided by the NSIDC. The sea ice type products were provided by the EUMETSAT OSI SAF. Funding for this project was provided by the National Key Research and Development Program of China (No. 2016YFC1402704), and the Global Change Research Program of China (No. 2015CB953901).

References

Ashcroft, P., and Wentz, F., 2013. AMSR-E/Aqua L2A global swath spatially-resampled brightness temperatures, version 3. NASA National Snow and Ice Data Center Distributed Active Archive Center, Boulder, Colorado, USA, DOI: 10.5067/AMSR-E/AE_L2A.003.

Brucker, L., and Markus, T., 2013. Arctic-scale assessment of satellite passive microwave-derived snow depth on sea ice using Operation IceBridge airborne data. *Journal of Geophysical Research: Oceans*, **118**: 2892-2905, DOI: 10.1002/jgrc.20228.

Cavalieri, D. J., Comiso, J. C., and Markus, T., 2014. AMSR-E/Aqua daily L3 12.5 km brightness temperature, sea ice concentration, and snow depth polar grids, version 3. NASA National Snow and Ice Data Center Distributed Active Archive Center, Boulder, Colorado, USA, DOI: 10.5067/AMSR-E/AE_SI12.003.

Cavalieri, D. J., Crawford, J., Drinkwater, M., Emery, W. J., Eppler, D. T., Farmer, L. D., Goodberlet, M., Jentz, R., Milman, A., Morris, C., Onstott, R., Schweiger, A., Shuchman, R., Steffen, K., Swift, C. T., Wackerman, C., and Weaver, R. L., 1992. NASA sea ice validation program for the DMSP SSMI: Final report. NASA Technical Memorandum 104559. National Aeronautics and Space Administration, Washington, D. C., USA.

Comiso, J. C., and Hall, D. K., 2014. Climate trends in the Arctic as observed from space. *WIREs Climate Change*, **5**: 389-409, DOI: 10.1029/JC091iC08p09663.

Comiso, J. C., and Sullivan, C. W., 1986. Satellite microwave and *in-situ* observations of the Weddell sea ice cover and its marginal ice zone. *Journal of Geophysical Research*, **91** (CS): 9663-9681, DOI: 10.1029/JC091iC08p09663.

Comiso, J. C., Cavalieri, D. J., and Markus, T., 2003. Sea ice concentration, ice temperature, and snow depth using AMSR-E data. *IEEE Transactions on Geoscience and Remote Sensing*, **41** (2): 243-252, DOI: 10.1109/TGRS.2002.808317.

Comiso, J. C., Cavalieri, D. J., Parkinson, C. L., and Gloersen, P., 1997. Passive microwave algorithms for sea ice concentration – A comparison of two techniques. *Remote Sensing of Environment*, **60** (3): 357-384, DOI: 10.1016/S0034-4257(96)00220-9.

Gloersen, P., and Barath, F. T., 1977. A scanning multichannel microwave radiometer for Nimbus-G and SeaSat-A. *IEEE Journal of Oceanic Engineering*, **2** (2): 172-178, DOI: 10.1109/joe.1977.1145331.

Gloersen, P., Campbell, W. J., Cavalieri, D. J., Comiso, J. C., Parkinson, C. L., and Zwally, H. J., 1992. Arctic and Antarctic sea ice, 1978–1987: Satellite passive microwave observations and analysis. *National Aeronautics and Space Administration*, **SP-511**: 200, DOI: 10.1016/0021-9169(95)90010-1.

Gloersen, P., Willicit, T. T., Chang, T. C., Nordberg, W., and Campbell, W. J., 1974. Microwave maps of the polar ice of

the Earth. *Bulletin of the American Meteorological Society*, **55**: 1442-1448.

Holland, M. M., and Bitz, C. M., 2003. Polar amplification of climate change in coupled models. *Climate Dynamics*, **21** (3-4): 221-232, DOI: 10.1007/s00382-003-0332-6.

Ivanova, N., Johannessen, O. M., Pedersen, L. T., and Tonboe, R. T., 2014. Retrieval of Arctic sea ice parameters by satellite passive microwave sensors: A comparison of eleven sea ice concentration algorithms. *IEEE Transactions on Geoscience and Remote Sensing*, **52** (11): 7233-7246, DOI: 10.1029/JC091iC03p03913.

Kaleschke, L., Lüpkes, C., Vihma, T., Haarpaintner, J., Bochert, A., Hartmann, J., and Heygster, G., 2001. SSM/I sea ice remote sensing for mesoscale ocean-atmosphere interaction analysis. *Canadian Journal of Remote Sensing*, **27** (5): 526-537, DOI: 10.1080/07038992.2001.10854892.

Kawanishi, T. J., Sezai, T., Ito, Y., Imaoka, K., Takeshima, T., Ishido, Y., Shibata, A., Miura, M., Inahata, H., and Spencer, R. W., 2003. The Advanced Scanning Microwave Radiometer for the Earth Observing System (AMSR-E): NASDA's contribution to the EOS for global energy and water cycle studies. *IEEE Transactions on Geoscience and Remote Sensing*, **41** (2): 184-194, DOI: 10.1109/TGRS.2002.808331.

Kelly, R., Chang, A. T. C., Tsang, L., and Foster, J. L., 2003. A prototype AMSR-E global snow area and snow depth algorithm. *IEEE Transactions on Geoscience and Remote Sensing*, **41** (2): 230-242, DOI: 10.1109/tgrs.2003.809118.

Kern, S., 2004. A new method for medium-resolution sea ice analysis using weather-influence corrected Special Sensor Microwave/Imager 85 GHz data. *International Journal of Remote Sensing*, **25** (21): 4555-4582, DOI: 10.1080/01431160410001698898.

Kurtz, N. T., Farrell, S. L., Studinger, M., Galin, N., Harbeck, J. P., Lindsay, R., Onana, V. D., Panzer, B., and Sonntag, J. G., 2013. Sea ice thickness, freeboard, and snow depth products from Operation IceBridge airborne data. *The Cryosphere*, **7**: 1035-1056, DOI: 10.5194/tc-7-1035-2013.

Kurtz, N. T., Studinger, M. S., Harbeck, J., Onana, V., and Yi, D., 2015. IceBridge L4 sea ice freeboard, snow depth, and thickness, version 1. NASA National Snow and Ice Data Center Distributed Active Archive Center, Boulder, Colorado, USA, DOI: 10.5067/G519SHCKWQV6.

Markus, T., and Cavalieri, D. J., 1998. Snow depth distribution over sea ice in the Southern Ocean from satellite passive microwave data. In: *Antarctic Sea Ice: Physical Processes, Interactions and Variability*. Jeffries, M. O., ed., American Geophysical Union, Washington, D. C., 19-40, DOI: 10.1029/AR074p0019.

Markus, T., and Cavalieri, D. J., 2000. An enhancement of the NASA team sea ice algorithm. *IEEE Transactions on Geoscience and Remote Sensing*, **38** (3): 1387-1398, DOI: 10.1109/36.843033.

Markus, T., and Cavalieri, D. J., 2008. *AMSR-E Algorithm Theoretical Basis Document Supplement: Sea Ice Products*. Hydrospheric and Biospheric Sciences Laboratory. NASA Goddard Space Flight Center, Greenbelt, MD, 1-9.

Markus, T., Comiso, J. C., Cavalieri, D. J., and Ivanoff, A., 2015. NRT AMSR2 daily L3 12.5 km TB and sea ice concentration polar grids. https://lance.nsstc.nasa.gov/amsr2-science/data/level3/seaice25. NASA Global Hydrology Center DAAC, Huntsville, Alabama, USA, DOI: 10.5067/AMSR2/A2_SI2 5_NRT.

Parkinson, C. L., Comiso, J. C., Zwally, H. J., Cavalieri, D. J., Gloersen, P., and Campbell, W. J., 1987. Arctic sea ice, 1973–1976: Satellite passive microwave observations. *National Aeronautics and Space Administration*, **SP-489**: 296.

Spreen, G., Kaleschke, L., and Heygster, G., 2008. Sea ice remote sensing using AMSR-E 89-GHz channels. *Journal of Geophysical Research*, **113** (C2): 447-453, DOI: 10.1029/2005JC003384.

Svendsen, E., Atzler, C. M., and Grenfell, T. C., 1987. A model for retrieving total sea ice concentration from a spaceborne dual-polarized passive microwave instrument operating near 90 GHz. *International Journal of Remote Sensing*, **8** (10): 1479-1487, DOI: 10.1080/01431168708954790.

Tschudi, M., Fowler, C., Maslanik, J., Stewart, J. S., and Meier, W., 2016. EASE-grid sea ice age, version 3. NASA National Snow and Ice Data Center Distributed Active Archive Center, Boulder, Colorado, USA, DOI: 10.5067/PFSVFZA9 Y85G.

Yang, H., Weng, F. Z., Lv, L. Q., Lu, N. M., Liu, G. F., Bai, M., Qian, Q. Y., He, J. K., and Xu, H. X., 2011. The FengYun-3 microwave radiation imager on-orbit verification. *IEEE Transactions on Geoscience and Remote Sensing*, **39** (11): 4552-4560, DOI: 10.1109/TGRS.2011.2148200.

Yang, H., Zou, X. L., Li, X. Q., and You, R., 2012. Environmental data records from FengYun-3B microwave radiation imager. *IEEE Transactions on Geoscience and Remote Sensing*, **50** (12): 4986-4993, DOI: 10.1109/tgrs.2012.2197003.

Zwally, H. J., Comiso, J. C., Parkinson, C. L., Campbell, W. J., Carsey, F. D., and Gloersen, P., 1983. *Antarctic Sea Ice, 1973–1976: Satellite Passive-Microwave Observations*. NASA SP-459, Washington, D. C., 1-206.

(Edited by Chen Wenwen)